ACS APPLIED MATERIALS & INTERFACES

www.acsami.org

Research Article

Organic Photovoltaic Pseudocapacitors for Neurostimulation

Mertcan Han, Shashi Bhushan Srivastava, Erdost Yildiz, Rustamzhon Melikov, Saliha Surme, Itir Bakis Dogru-Yuksel, Ibrahim Halil Kavakli, Afsun Sahin, and Sedat Nizamoglu*

Cite This: ACS Appl. Mater. Interfaces 2020, 12, 42997−43008

Read Online

ACCESS | Metrics & More | Article Recommendations | Supporting Information

ABSTRACT: Neural interfaces are the fundamental tools to understand the brain and cure many nervous-system diseases. For proper interfacing, seamless integration, efficient and safe digital-to-biological signal transduction, and long operational lifetime are required. Here, we devised a wireless optoelectronic pseudocapacitor converting the optical energy to safe capacitive currents by dissociating the photogenerated excitons in the photovoltaic unit and effectively routing the holes to the supercapacitor electrode and the pseudocapacitive electrode−electrolyte interfacial layer of PEDOT:PSS for reversible faradic reactions. The biointerface showed high peak capacitive currents of ∼3 mA·cm^{-2} with total charge injection of ∼1 μC·cm^{-2} at responsivity of 30 mA·W^{-1}, generating high photovoltages over 400 mV for the main eye photoreception colors of blue, green, and red. Moreover, modification of PEDOT:PSS controls the charging/discharging phases leading to rapid capacitive photoresponse of 50 μs and effective membrane depolarization at the single-cell level. The neural interface has a device lifetime of over 1.5 years in the aqueous environment and showed stability without significant performance decrease after sterilization steps. Our results demonstrate that adopting the pseudocapacitance phenomenon on organic photovoltaics paves an ultraefficient, safe, and robust way toward communicating with biological systems.

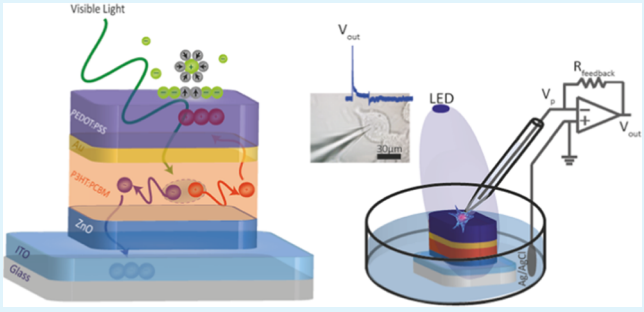

KEYWORDS: *neurostimulation, organic photovoltaics, bioelectronics, pseudocapacitors, PEDOT:PSS*

INTRODUCTION

Stimulation of nerve tissue is an essential tool in neurotherapeutics, neural prosthetics, and biomedical research.[1] Semiconductor and metal devices were already used as stimulation platforms in deep-brain stimulation to regulate brain activity and in neuroscientific research to recognize complex neural networks. However, the spatial resolution of the stimulating currents limits their efficacy and the electrical wiring of these devices also introduces difficulty in surgery.[2−6] Alternatively, photovoltaic stimulation eliminates the need for electrical wiring, which makes it a powerful and less invasive alternative to electrode-based devices used in the last decade.[7,8] Moreover, it reduces device−tissue mechanical mismatch, which is an obstacle for metal or bulk silicon devices as the rigidness causes scar tissue formation and contact problems with biological tissues.[6,9]

In organic photovoltaic platforms, stimulation is achieved by the faradic,[10,11] photothermal,[12] or capacitive[13] phenomenon. Among these stimulation mechanisms, the capacitive mechanism is based on the perturbation of the ions in the electrolyte/electrode interface and generates stimulating potential fields on the cell membrane. This offers a rapid and safe charge-injection mechanism for cell stimulation due to suppressed redox reactions and heating effect. In terms of capacitive organic biointerfaces, so far organic pigments such as indigo,[14] pi-conjugated polymers,[15] p−n semiconducting organic nanocrystals,[16] and quantum dot integrated organic polymers[17,18] have been used to generate capacitive photocurrents. These biointerfaces utilized double-layer capacitance for capacitive neuromodulation.

One promising approach increasing the capacitive current can be adaptation of the supercapacitor technology to organic biointerfaces. In addition to the double-layer capacitance, supercapacitors advantageously introduce the pseudocapacitance based on fast and reversible redox reactions. In these devices, the pseudocapacitance can be more than 2 orders of magnitude higher than the double layer and significantly increase the total interfacial capacitance.[19] In organic supercapacitors, this is achieved by the electron-charge transfer between the electrolyte solution and the electrode originated from an adsorbed ion. The ion does not form a chemical bond as only charge transfer occurs in charging. The reactions are

Received: June 26, 2020
Accepted: August 27, 2020
Published: August 27, 2020

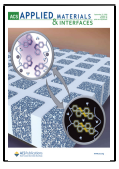

https://dx.doi.org/10.1021/acsami.0c11581
ACS Appl. Mater. Interfaces 2020, 12, 42997−43008

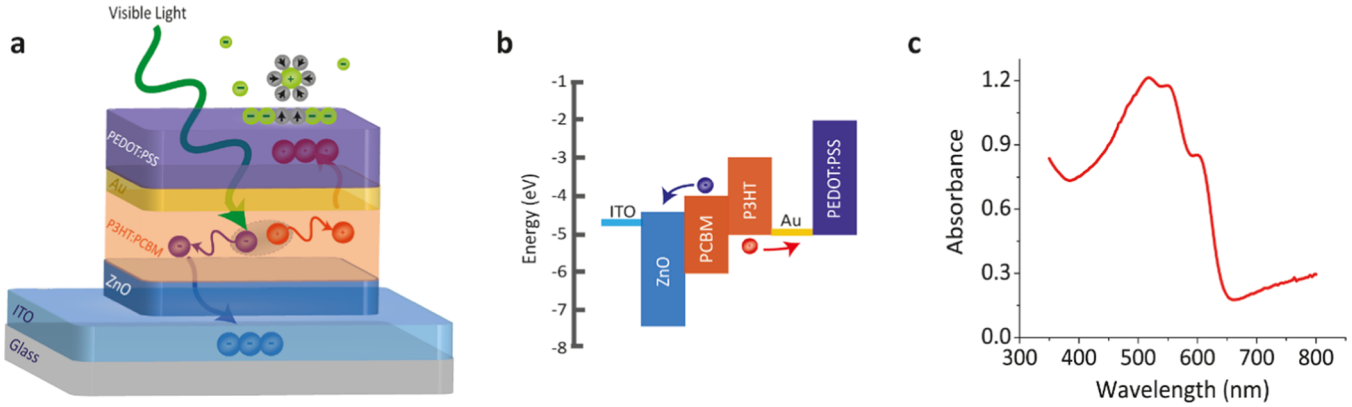

Figure 1. Device architecture and material characteristics. (a) Structure of the organic photovoltaic pseudocapacitor biointerface. It incorporates a photovoltaic unit composed of ITO/ZnO/P3HT:PCBM and a pseudocapacitor made of Au/PEDOT:PSS. Light stimulation in the photovoltaic unit causes charge separation in the photoactive layer. Au was used as the hole collector, and PEDOT:PSS operates as the pseudocapacitive interfacial layer to host polarized solvent molecules and also specifically adsorb ions for reversible faradic reactions. (b) Energy band diagram of the organic photovoltaic pseudocapacitor. (c) Ultraviolet-to-visible absorption spectrum of the biointerface.

reversed after the discharge, which secures from the introduction of any toxic material or pH change to the cellular environment.

Here, we report a neural interface combining pseudocapacitors with organic photovoltaics for safe and efficient photostimulation of neurons. For that, a bulk heterojunction photovoltaic unit is integrated with a supercapacitor electrode where Au acts as a hole collector and PEDOT:PSS acts as the pseudocapacitive interfacial layer that hosts polarized solvent molecules and specifically adsorbed ions via reversible faradic reactions (Figure 1a). The band alignment match of the highest occupied molecular orbital (HOMO) levels facilitates effective routing of holes to the PEDOT:PSS for efficient conversion of light-to-capacitive currents. This leads to a fast photoresponse of 50 μs for high-speed communication with living systems and high current peaks of ~3 mA·cm^{-2} with total charge injection of ~1 μC·cm^{-2} at a responsivity of 30 mA·W^{-1}. Moreover, the neural interface simultaneously offers seamless biointegration via wireless operation; broadband visible communication covering blue, green, and red spectral regions; long operation lifetime over 1.5 years in an aqueous environment; stability without any visible delamination or significant performance decrease after sterilization steps under UV and ethanol treatments; and biocompatibility due to incorporation of nontoxic materials. Furthermore, the charging/discharging of capacitive current can be tuned by changing the additive concentration of the PEDOT:PSS, which leads to the control of the transmembrane depolarization/hyperpolarization phases at the single-cell level.

RESULTS

Principle of the Biointerface Design, Architecture, and Operation. The photovoltaic pseudocapacitor was fabricated by successive deposition of multiple layers onto indium tin oxide (ITO)-coated glass substrates in the following order: zinc oxide (ZnO), poly(3-hexylthiophene-2,5-diyl):[6,6]-phenyl-C61-butyric acid methyl ester (P3HT:PCBM), gold (Au), and PEDOT:PSS (Figure 1a). Formation of the architecture requires a pseudocapacitive surface material for fast reversible redox reactions. For that, we selected PEDOT doped with PSS (PEDOT:PSS), which has been widely used for organic bioelectronics due to its water dispersibility, ease to be coated as thin films, environmental stability, biocompatibility, and mechanical flexibility.[20] Moreover, PEDOT:PSS, known for its high electrolytic capacitance, is advantageous to be used in an electronic system because of its electrical tunability, high hole mobility, and conductivity.[21] Since a charge collector should be placed near the conductive polymer electrode, the Au layer was used with PEDOT:PSS side by side,[22] which is also used in microelectrode arrays to record neural activity.[23,24] Au was chosen because of its work function match with the HOMO level of the PEDOT:PSS for hole collection (Figure 1b). Moreover, in our design, the charge collector work function needs to also match with the HOMO level of the photoactive layer to collect dissociated holes. Hence, Au is a well-matched bridging material satisfying both requirements.

The P3HT and PCBM conjugated polymer blend, which has absorbance in the visible spectrum (Figure 1c), was used as the photoactive layer for charge dissociation and recollection. We enhanced crystallinity of the photoactive layer by annealing, which also simultaneously leads to improvement in the surface morphology, increase in the charge generation efficiency, and elimination of any residual solvents. To promote effective charge separation in the photovoltaic unit (Figure 1a), the hole blocker layer ZnO was utilized, which further dissociates the electrons and holes and mainly guides electrons toward the transparent ITO electrode.[25] Moreover, the band alignment also facilitated the accumulation of holes to the PEDOT:PSS (Figure 1b). Then, the holes in the PEDOT:PSS interfacial layer attracted solvated ions in the electrolyte (Figure 1a). This ion attraction stimulates electron-charge transfer between the electrolyte and PEDOT:PSS layer. Reversible faradic reactions occur on the surface of the PEDOT:PSS layer (Figure 1a). Since the HOMO energy of PEDOT:PSS is higher than the water oxidation energy, any hole-based nonreversible faradic current generation is limited, which makes it a convenient candidate as a photovoltaic system using pseudocapacitance.

Conductivity and Stability Optimization by Chemical Modification of PEDOT:PSS. For the proper operation of the pseudocapacitor, the surface layer of PEDOT:PSS needs to be properly engineered in terms of solubility and conductivity. Water solubility and weak cohesion of the PEDOT:PSS are the main barriers over its potential to be used in aqueous environments, particularly in biological tissues. For this reason, it was mostly used as a noninterfacial layer in previous

https://dx.doi.org/10.1021/acsami.0c11581
ACS Appl. Mater. Interfaces 2020, 12, 42997−43008

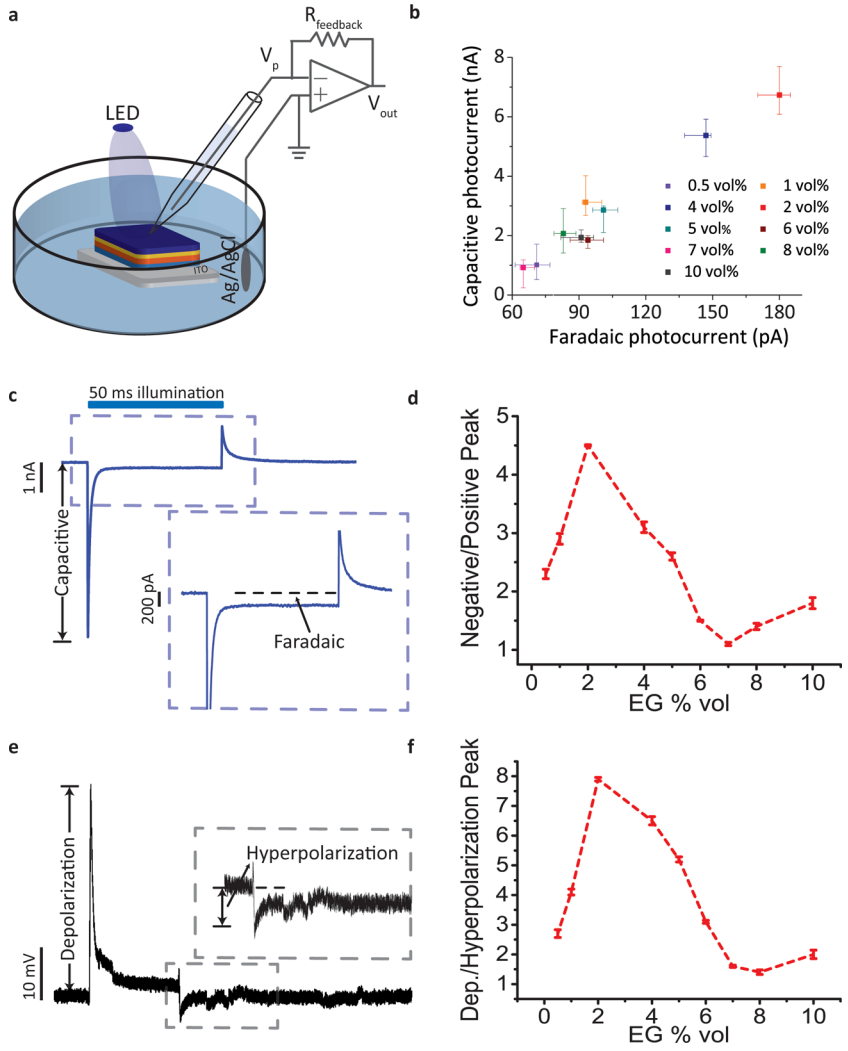

Figure 2. Chemical tuning of the capacitive and faradic parts of the photoresponse. (a) Schematic of the photocurrent measurement system. A patch-clamp electrophysiological recording system was used. Photoelectrodes were placed in the free-standing mode to mimic the behavior in biological media. The pipette was positioned close to the surface of the biointerface. The ITO layer that is in direct contact with the electrolyte was used as the return electrode. (b) Capacitive and faradic parts of the total photocurrent with different EG ratios in the PEDOT:PSS solution (n = 6). (c) Representative photoresponse of the Au/PEDOT:PSS-coated biointerface to define capacitive and faradic parts of the photocurrents. The blue area on the top shows the light illumination period. The blue dashed box marks the region shown in the inset. (d) Negative and positive absolute photocurrent peak ratios with different EG ratios (n = 6). (e) Representative cellular photoresponse generated by the biointerface. The gray dashed box marks the region shown in the inset. (f) Ratio of depolarization and hyperpolarization for different EG ratios (n = 6). All data are presented as means ± standard error of the mean (SEM).

studies.[26] Also, the electrical conductivity of PEDOT:PSS is low for high-current organic photovoltaics because of the phase segregation and insulating effect of the PSS components that limit the connectivity between conductive PEDOT domains.[25] Since the electrochemical activity and ion transport between the PEDOT chain and the PSS network are based on hydrated pathways, decreasing the water solubility causes a significant decrease in electrical conductivity.[22] Hence, low water solubility while having high conductivity is required.

We investigated different ratios of ethylene glycol (EG), dimethyl sulfoxide (DMSO), and 3-glycidoxypropyltrimethoxysilane (GOPS) to enhance the integrity of PEDOT:PSS films in aqueous environments and to build mechanically robust, stable, and efficient bioelectronic devices with a PEDOT:PSS interface. The silane-based cross-linking agent, GOPS, was used to increase aqueous stability. However, it also increases electrochemical impedance and decreases electrical conductivity.[27] These drawbacks can be compensated by co-optimization of the cross-linker with the conductivity enhancers, EG and DMSO. The effect of weight percentage of DMSO in the PEDOT:PSS solution can increase film cohesion, electrical conductivity, and current efficiency.[28] Likewise, the addition of the polar solvent EG can enhance electrical conductivity and change the PEDOT:PSS film morphology by aggregating PEDOT:PSS particles and increasing surface roughness. This is also beneficial to increase interfacial capacitance by improving the impregnation of the insulating environment and providing a proper interface for cell attachment and growth.

To observe the biointerface stability in aqueous environments and to test its potential use as an electrophysiological stimulation platform, we measured photocurrent generation and investigated biointerface integrity at various concentration levels of the cross-linking agent GOPS (0, 0.5, 1, 2, 3, and 5 wt %) in PEDOT:PSS. The photocurrent was measured between

https://dx.doi.org/10.1021/acsami.0c11581
ACS Appl. Mater. Interfaces 2020, 12, 42997−43008

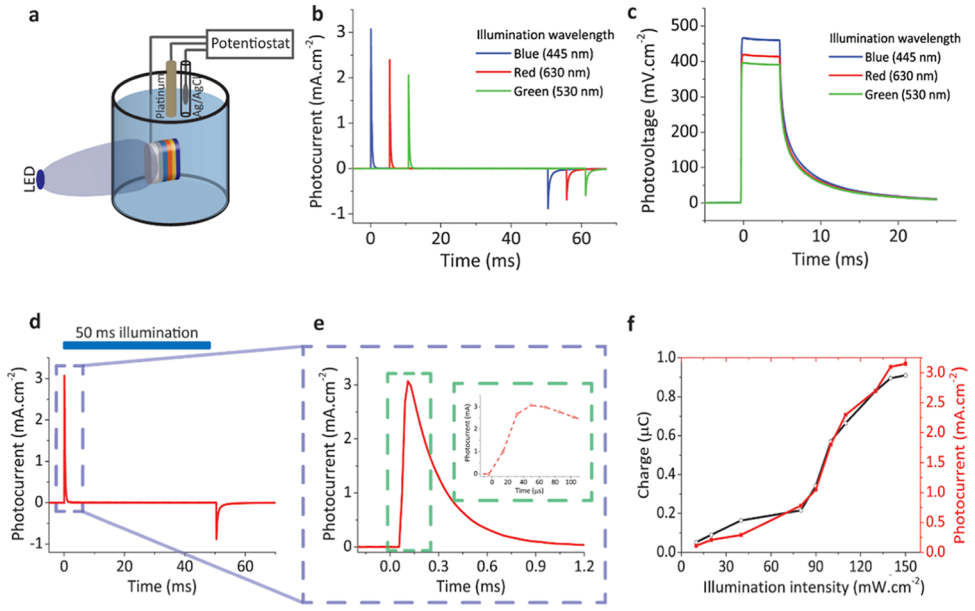

Figure 3. Photoelectrochemical characterization of the biointerface to explore benchmark values. (a) Schematic of the photoelectrochemical measurement system. A potentiostat module combined with platinum and Ag/AgCl electrodes was utilized for the measurement. The working electrode was directly connected to the ITO layer with a metal clip as the return electrode in the system. The device area of ∼1 cm^2 was illuminated. (b) Photocurrent and (c) photovoltage transient response under the illumination of 445, 530, and 630 nm light pulses with trains of 50 ms, 100 $mW{\cdot}cm^{-2}$. (d) Best photocurrent performance under blue light illumination (445 nm). The blue area on the top shows the light illumination period. The blue dashed box marks the region shown in (e). (e) Closeup for photocurrent transient; the green dashed box marks the region shown in the inset to identify the rise time. (f) Photocurrent and charge generation correlation with respect to different illumination powers using 445 nm blue light-emitting diode (LED).

the distant Ag/AgCl bath electrode[29] and a glass capillary electrode in artificial cerebrospinal fluid (Figure 2a). Although photocurrent generation was maximized with 0 and 0.5 wt % GOPS contents, the interfacial layer dissolved in the biological medium and damaged the device in a few minutes. In contrast, when GOPS increases, the conductivity decreases. Since there is a trade-off between the biointerface integrity and conductivity, we chose 1 wt % GOPS as the proper concentration to obtain aqueous stability without significant decrease of conductivity.

Tuning of Charge and Discharge Phases. Next, we investigated the effect of EG concentration on capacitive and faradic photocurrents while keeping GOPS and DMSO constant (as 1 wt % and 7 vol %), respectively (Figure 2b,c). Then, 2 vol % EG concentration showed the highest capacitive photocurrent level under the same light intensity levels. Since a balanced capacitive process with symmetric charging and discharging current phases might be preferred,[30] EG concentration of 7 vol % that has the peak ratio of 1.1 can satisfy such a symmetric photocurrent profile. Furthermore, we achieved a controllable way to regulate photocurrent generation during these phases by tuning electrical properties of the PEDOT:PSS solution via varying the EG concentration from 0.5 to 10 vol % while keeping the biointerface structure fixed. Unbalanced capacitive waveforms are also used for neurostimulation of cells as well,[16] and for that purpose, the EG concentration of 2 vol % can lead to negative and positive photocurrent peak ratio of 4.5 (Figure 2d). The effect of negative and positive capacitive peaks on depolarization and hyperpolarization of peak ratios on SHY-5Y cells was also investigated (Figure 2e,f). According to the extracellular two-dimensional (2D) stimulation model by Fromherz,[31] since the capacitive currents that are injected to the cells though are partially leaked to the cleft, the capacitive current pattern needs to be proportional to the membrane potential change. As a result, they showed a similar trend to negative/positive photocurrent peak ratios in photocurrent measurements (Figure 2f). Different from the previous studies, our biointerface shows selective control over peak photocurrent and total injected charge for both charging and discharging phases. We achieved a clear control over charging/discharging photocurrent peaks and total injected charges with the modifications on PEDOT:PSS.

Photocurrent and Photovoltage Generation. To investigate the contribution of the Au/PEDOT:PSS layer to the biointerface, we characterized the photocurrent generation by the optimized ITO/ZnO/P3HT:PCBM/Au/PEDOT:PSS (biointerface) and ITO/ZnO/P3HT:PCBM (control) structures, respectively. We used a three-electrode photoelectrochemical measurement technique to obtain photoresponse using chronoamperometry and chronopotentiometry measurements (Figure 3a). This experiment was carried out in aCSF solution with 50 ms pulsed illumination using blue, red, and green LEDs used in photocurrent measurements, ∼100 $mW{\cdot}cm^{-2}$ at a frequency of 2 Hz with a device illumination area of ∼1 cm^2. Although 0.1 M KCl electrolyte solution could be used to obtain the highest benchmark values of the biointerface, using aCSF solution is a convenient way to mimic and test in the biological environment. Chronoamperometry measurements revealed that our biointerface can generate ∼3.1 $mA{\cdot}cm^{-2}$ (Figure 3b). Moreover, photocurrent response has a highly capacitive nature with only <1% faradic contribution.[12] To obtain photovoltage benchmark values for our device, chronopotentiometry measurements revealed that the biointerface can generate ∼470 mV under 445 nm illumination with power of ∼100 $mW{\cdot}cm^{-2}$ (Figure 3c). The

https://dx.doi.org/10.1021/acsami.0c11581
ACS Appl. Mater. Interfaces 2020, 12, 42997−43008

performance of the biointerface under blue light with 470 mV photovoltage exceeds the photovoltage levels in recent photocapacitor architectures[14,16,32] and even higher than ~400 mV under green and red illumination as well (Figure 3c). Therefore, the biointerface can operate within the visible spectrum with high performance. Since the tissue transparency window is between 620 and 800 nm, having high-performance benchmark values in red is important for stimulation through brain and skin tissues.[33] Moreover, the biointerface showed fast charging and discharging phases, revealing themselves in chronoamperometry measurements (Figure 3d,e). The rise time for the charging phase corresponds to ~50 μs (Figure 3e, inset), which is well-suited for high-frequency neuromodulation applications. The total charge injection was calculated by integrating the photocurrent transient as 0.9 μC·cm^{-2}. The injected charge level is comparable to the threshold charge density for neural prostheses,[34] and even under this low light intensity, the charge injection was on the order of μC·cm^{-2} (Figure 3f).

To further investigate the photoelectric response, a patch-clamp system was used. Incorporation of the Au/PEDOT:PSS layer facilitated an increase of the peak photocurrent of 2.3-fold in comparison with the control at the intensity level of 150 mW·cm^{-2}. Moreover, photoresponse of the biointerface did not exhibit a significant faradic photocurrent generation. In the optimized device, the faradic photocurrent level corresponds to 180 pA, which is less than 3% of the peak photocurrent (Figure 4a). As seen from the closeup charging peak (Figure 4a), the photocurrent peak is higher, while the decay time is also longer for Au/PEDOT:PSS-coated biointerfaces. Longer decay time reveals that device capacitance is higher since the discharging phase depends on the device's RC time constant. Furthermore, the photoresponse of our biointerface showed highly photocapacitive processes under not just excitation in blue but also in green and red windows (Figure 4b). These results are promising for photostimulation with different illumination colors as well as white light.

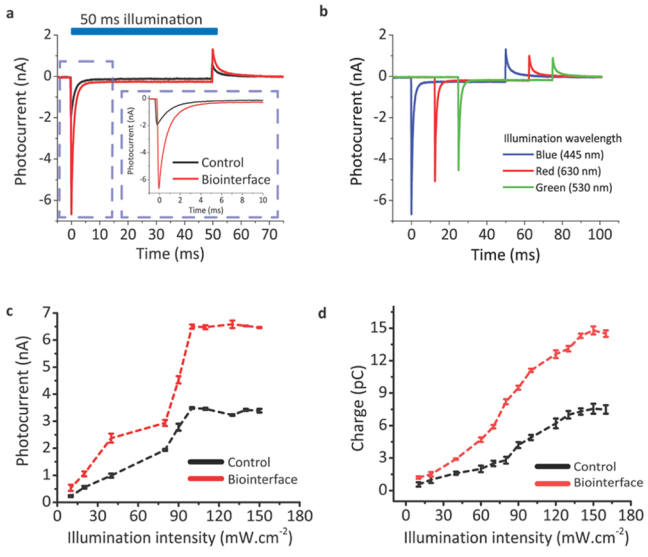

Figure 4. Photocurrent measurements to identify the spectral response and total charge injection. (a) Photocurrent response upon illumination with trains of 50 ms, 120 mW·cm^{-2} light pulses for the control (black) and Au/PEDOT:PSS-coated biointerfaces (red). The blue area on the top shows the light illumination period. The blue dashed box marks the region shown in the inset to identify capacitive and faradic parts of the photocurrent. (b) Spectral photoresponse of the biointerface under 445, 530, and 630 nm light pulses with trains of 50 ms, 100 mW·cm^{-2}. (c) Photocurrent peaks under different illumination powers (n = 6). (d) Charge injection amounts under different illumination powers (n = 6). All data in (c) and (d) are presented as means ± SEM.

Photocurrent enhancement levels due to the Au/PEDOT:PSS layer is further characterized at different intensity levels with a second set of experiments (Figure 4c,d). For illumination powers larger than 100 mW, the peak photocurrent started to saturate around 6.5 nA and peak photocurrents were found as 6.6 ± 0.2 nA under 120 mW·cm^{-2} illumination (Figure 4c). A mean ~2.3-fold enhancement was observed up to the intensity level of 150 mW·cm^{-2}. The injected charge was again analyzed by integrating the photocurrent transient response (Figure 4d), and a maximum charge injection of 15 pC is observed at the light intensity level of 150 mW·cm^{-2}. The charge injection was higher for the biointerface for each illumination power, and the total injected charge also increased more than 2.5-fold at the light intensity level of 150 mW·cm^{-2} in comparison with the control. Here, the increase of the charge injection corresponding to 2.5-fold is larger than the peak current levels due to the longer discharging time of the biointerface. The faradic current ratio for all light intensity levels was at a similar level of <3%. Therefore, both the peak photocurrent and injected charge are strongly increased without any compromise due to faradic charge generation at higher intensity levels. The notable increase in photocurrent generation and charge injection is mainly due to the high electrolytic capacitance of PEDOT:PSS and incorporation of Au, which also have well-matched HOMO levels for effective hole transport. Moreover, to evaluate the effective stimulation distance, the photocurrent gradient is measured for increasing the distance between the patch pipette and the biointerface−electrolyte interface. Even for 125 μm distance from the surface, which is longer than the targeted cell dimensions, the photocurrent is highly retained by 90%, and the exponential decrease in photocurrent gradient (Figure S1) shows that charge accumulation is confined at the interface upon illumination.

Photostability and Biocompatibility. For biomedical applications, stability is an important factor limiting the functionality of the implants. We apply stability tests for the optimized biointerface structure. To simulate the environment in biological tissues, biointerfaces were kept completely immersed in aCSF solution and photocurrent was measured periodically for 60 days. The recorded peak photocurrent density only decreased by 9.2% after 60 days, relative to the first day, which corresponds to a device half-time of ~1.8 years in an aqueous environment (n = 10). Furthermore, to investigate the effect of the sterilization process on biointerface performance, we carried out accelerated stress tests. The test includes sequential treatments of UV sterilization for 30 min, quadruple treatment with absolute ethanol, overnight incubation in aCSF medium, a second UV sterilization for 30 min, and quadruple treatment with absolute ethanol. After these treatments, photocurrent and total charge generation only showed a 4% decrease in the photocurrent peak and a 6% decrease in the total injected charge, respectively. Therefore, our biointerface configuration proved its stability without any visible delamination or significant performance decrease after sterilization steps.

https://dx.doi.org/10.1021/acsami.0c11581
ACS Appl. Mater. Interfaces 2020, 12, 42997−43008

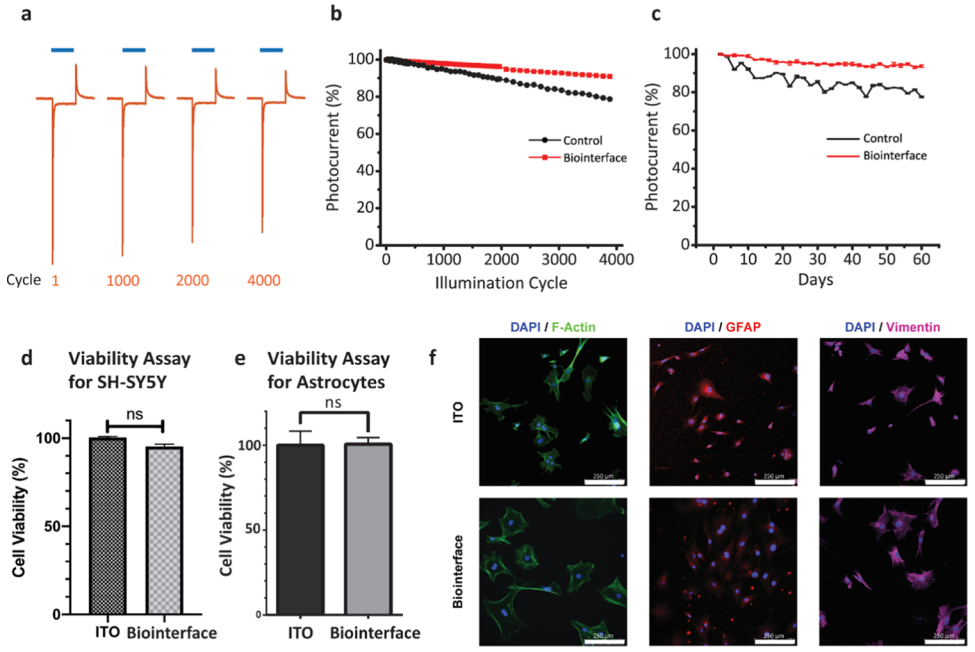

Figure 5. Cyclic and continuous photostability tests and biocompatibility experiments. (a) Device stability in the biological medium. Biointerfaces were kept in aCSF for 60 days, and on each of the two days, photocurrent measurements were repeated to evaluate device stability in the biological medium (aCSF). Blue areas on the top highlight the light illumination periods. Blue bars represent 50 ms illumination using a blue LED with nominal wavelength at 445 nm, 120 mW·cm^{-2} power. (b) Peak value of the photocurrent transient over 4000 cyclic illumination cycles for the control and the biointerface. Photocurrent peaks were normalized with respect to the value in the first cycle. (c) Time-dependent cyclic stability. Photocurrent peaks were measured in periodic cyclic illumination, and measurements were normalized to analyze photostability over 60 days. (d) Effect of two types of biointerfaces on cell metabolic activity was assessed by the MTT assay and compared with the ITO control. An unpaired two-tailed *t*-test was performed to determine the level of significance. Each experiment was carried out with at least three biological replicates (n = 3). *p < 0.05 was considered statistically significant, and nonsignificant differences are presented as "ns". (e) Viability assay for primary astrocytes on the biointerface compared with the ITO control. An unpaired two-tailed *t*-test was performed to determine the level of significance. Each experiment was carried out with at least three biological replicates (n = 3). *p < 0.05 was considered as statistically significant, and nonsignificant differences are presented as ns. (f) Immunofluorescence images of primary astrocytes on ITO control and the biointerface. Primary astrocytes co-stained with DAPI and F-Actin, GFAP, Vimentin antibodies, respectively (scale bars: 250 μm).

Another important criterion for implantable and optically stimulated devices is the photocurrent retention after exposing cyclic and continuous light illumination.[12] To explore the effect of cyclic illumination, photocurrent generation was measured during 4000 cycles of illumination using a blue LED (445 nm nominal wavelength), 50 ms, ∼100 mW·cm^{-2} at the frequency of 1 Hz (n = 10) (Figure 5a,b). In comparison to the control device with 78% retention, the Au/PEDOT:PSS-coated biointerface showed a higher retention by 94% after 60 days (Figure 5c). After cyclic illumination tests, devices were exposed to continuous illumination for 20 h using a blue LED (445 nm nominal wavelength) with ∼100 mW·cm^{-2} power (n = 10). Photocurrent generation of the biointerface again showed 84% conservation of the photocurrent peak after continuous illumination. For the control device, after 4000 cycles, the faradic part of the photocurrent decreased by 34%, and after 60 days, it reduced by 22%. The decrease in faradic contribution supports the capacitive charge generation claims.

Before testing the biointerface performance with neural cells, we conducted cell viability measurements using 3-(4,5-dimethylthiazol-2-yl)-2,5-diphenyl tetrazolium bromide (MTT) to investigate the biocompatibility of the device. SH-SY5Y cells grown on our biointerface have high viability with ITO substrates by 95% (Figure 5d). Furthermore, to evaluate the cell morphologies, DAPI and tubulin immunostaining experiments were carried out. The morphologies of the cells were similar on both the ITO control substrates (Figure S2a) and the biointerface (Figure S2b). Also, we conducted an MTT viability assay with primary astrocytes to investigate the innate immune response to the device. The population of primary astrocytes neither decreases nor increases significantly compared to the control group (Figure 5e). In addition to the viability assay, we observed astrocytes under phase-contrast (Figure S3) and immunofluorescence microscopes. We did not observe reactive astrocyte morphology in any of the samples (Figure 5f). Moreover, astrocytes well tolerated the stiffness of the interfacial surface[35] (Figure S3). These results indicate that our biointerface did not exhibit significant toxic and immune reactive effects to the cells *in vitro*, which was also expected since the device was composed of materials proven to be biocompatible.[36]

Neural Photostimulation. Finally, we investigated the neuromodulation ability of the optimized biointerface. We conducted our electrophysiological experiment on a model cell line, SH-SY5Y cells. These types of cell lines, like *Xenopus laevis* oocyte, Neuro2A, and SH-SY5Y cells, grant a stable testing platform to explore the neurostimulation capabilities and capacitive coupling between the biointerface and the cells and are used in a wide variety of *in vitro* studies.[11,32,37−39] SH-SY5Y cells were grown on the photoelectrodes, and they were approximately 30 μm in diameter (Figure 6a inset). First, the IV characteristic of SH-SY5Y cells on the biointerface was measured under dark conditions, revealing that the cells have a typical resting membrane potential around −50 mV (Figure

https://dx.doi.org/10.1021/acsami.0c11581
ACS Appl. Mater. Interfaces 2020, 12, 42997−43008

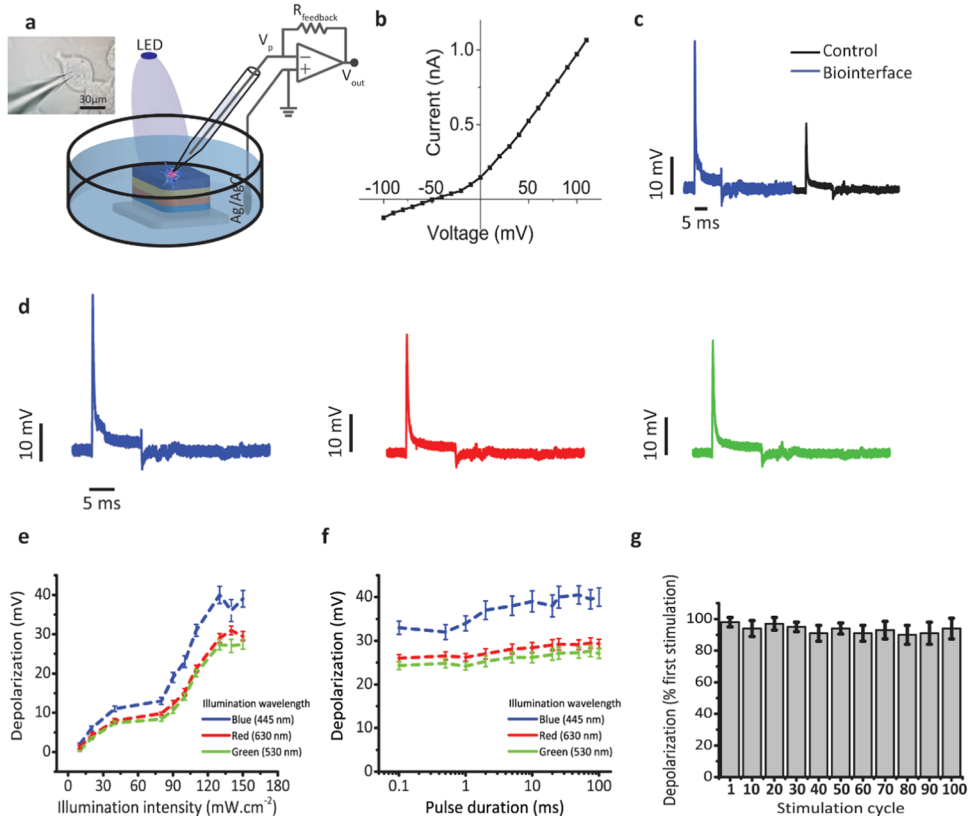

Figure 6. Neural stimulation experiments at the single-cell level. (a) Schematic of the electrophysiology patch-clamp measurement setup. Material thickness is not in scale. Left inset: image of the patch-clamped SH-SY5Y cell (scale bar: 30 μm). (b) $I-V$ curve of a measured SH-SY5Y cell. (c) Photostimulation of the SH-SY5Y cell on the control and the biointerface under illumination of 120 mW·cm^{-2} with 10 ms illumination pulses. Intracellular membrane potential with respect to a distant Ag/AgCl electrode was measured. (d) Photostimulation response of SH-SY5Y cells on the biointerface under 445, 530, and 630 nm light pulses with trains of 10 ms, 100 mW·cm^{-2}. (e) Depolarization amplitude for different illumination intensities of blue, red, and green lights (n = 10). (f) Depolarization amplitude for different pulse durations of blue, red, and green lights (n = 10). (g) Dependence of depolarization on the stimulus cycles. For each measurement cycle, the depolarization amplitudes were normalized with respect to the depolarization value upon the first stimulus (n = 10). All data in (e)−(g) are presented as means ± SEM.

6b). The intracellular membrane potential with respect to a distant Ag/AgCl bath electrode was measured by whole-cell patch-clamp recording[29] under different illumination powers from 10 to 150 mW·cm^{-2} (Figure 6a). Since the photocurrent generation is from the biointerface to the electrolyte in the attached membrane, initial hyperpolarization of the attached membrane and depolarization in the free cell membrane are expected to be observed. Recordings indicated an initial quick depolarization just after the illumination and hyperpolarization after the termination of the illumination (Figure 6c). The membrane potential almost reduced to the resting potential after 3.6 ms. The biointerface can generate ∼41 mV intracellular membrane potential change. Blue-light illumination caused 2-fold higher photocurrent generation and correspondingly higher membrane voltage change in comparison with the control (Figure 6c). Furthermore, to explore the color-dependent membrane potential, changes under LED illumination with three different wavelengths of 445, 530, and 630 nm were measured. Similar to the photocurrent measurements, membrane potential response showed a similar relative behavior to blue, green, and red lights (comparing Figures 3b,c and 6d). Depolarization levels under different light intensities prove that sufficient charge injection is achieved even under low intensities <100 mW·cm^{-2} (Figure 6e). Advantageously, the biointerface can generate depolarization of the cell membrane even with a stimulation pulse width of 0.1 ms, and depolarization levels show steady behaviors between 0.1 and 100 ms pulse widths of 445, 530, and 630 nm stimulating light (Figure 6f). Therefore, our design shows high stimulation performance under low light intensities as well as in blue, green, and red windows. Moreover, robust depolarization levels were achieved under various pulse widths. Though the cell viability experiments show high biocompatibility of the biointerface, it is essential to investigate the depolarization behavior after cyclic stimulation. The depolarization amplitudes among 100 stimulation cycles showed high retention of 93.46 ± 4.86% with respect to the initial depolarization upon the first stimulation (Figure 6g). This indicates the absence of undesired cellular responses and oxidative damage to the cells.

In comparison with the recent neural stimulation studies, we observed that the injected photocurrent amounts and variation of the intracellular membrane potential are sufficient to elicit action potential on primary neurons extracted from animals.[26,40] The voltage-gated sodium channel is mainly responsible for the depolarization phase. Around 8 pC charge generation, recorded in the patch-clamp setup, is necessary to open sodium-ion channels.[38] Since our biointerface can generate more than 12 pC (Figure 4d), it is sufficient to evoke action potentials. The photoelectrochemical measurements reveal that the biointerface can generate ∼1 μC charges, which is also sufficient for photostimulation.[34] Furthermore, extracellular photocapacitors, having <400 mV photovoltage

https://dx.doi.org/10.1021/acsami.0c11581
ACS Appl. Mater. Interfaces 2020, 12, 42997−43008

and <1 mA photocurrent generation,[32] were demonstrated to generate action potentials, and our biointerface can generate comparable levels as well.

Organic devices may also stimulate the neurons via thermocapacitive and photothermal effects. These effects may induce depolarization due to phase transition in the phospholipid ordering or induce hyperpolarization because of the changes in the membrane capacitance. To analyze the contribution of the thermal effect, we calculated the temperature induced by light illumination.[12,39] The maximum temperature that can be produced for 100 mW·cm^{-2} is less than 0.8 °C, which is lower than the required temperature change to generate photothermal current (Appendix 1). Therefore, in our design, photostimulated depolarization is dominantly based on photocapacitive mechanisms since faradic contribution to total photocurrent generation is limited to 3% and thermal effects are negligible.

DISCUSSION AND CONCLUSIONS

Inspired by supercapacitor technology, we showed an optoelectronic neural interface that integrates a photovoltaic unit with a pseudocapacitor. The well-matched energy band profile together with pseudocapacitance significantly increased the capacitive current levels in comparison with the control photocapacitor structure that only uses double-layer capacitance. Adapting Au and PEDOT:PSS together as a pseudocapacitive unit enhanced the hole accumulation toward the cell/device interface to facilitate reversible faradic reactions. Second, we showed that the tunability of charging and discharging phases of the capacitive photoresponse by chemically modifying the PEDOT:PSS layer enabled a high-level control over the cellular depolarization and hyperpolarization phases without changing the biointerface architecture. Moreover, the biointerface also showed strong photoresponse under the main eye-sensitivity colors of blue, green, and red. Hence, the integration of pseudocapacitors with organic photovoltaics points out an efficient, configurable, and broadband information-exchange ability with living systems.

The biointerface also indicates a safe and long-term communication way with cells. The operation mechanism of the biointerface is based on capacitive charge transfer that uses the perturbation of the ion concentration and reversible ionic reactions. Since the faradic contribution is low, the neuromodulation method of the biointerface can be safely used for long-term stimulation of neurons. Furthermore, the biointerface did not show any significant toxicity due to the biocompatible material content, and the wireless structure is another advantage for simpler surgery without wire-related complications. Also, our biointerface did not induce innate immune response on the astrocytes, which are the responsible cells for fibrosis and neuroinflammation, indicating that our biointerface will not encounter inflammation-related chronic rejection response in neural tissues.[41] The biointerface had durability in the biological environment, and it showed robust photoresponse after accelerated stress, cyclic, and continuous illumination tests. Due to the solution processability, ∼0.5 μm overall layer thickness, and having mechanically robust compounds,[24,26,42,43] it has high potential to be adapted in planar and pixelated implants and nervous therapeutics.

A broad range of neural interface architectures can be envisioned by combining photovoltaics and supercapacitors. Advantageously, a wide variety of organic materials such as polyaniline (PANI), polypyrrol (PPy), and polythiophene (PTh)[44] or nanomaterials such as oxides of transition metals like ruthenium oxide (RuO_2)[19] can be integrated into the device structures. Moreover, these biointerfaces can be used for various applications. For example, high photovoltage levels under illumination powers within ocular safety limits show promise for future retinal prosthetics. The incorporation of materials that have photoresponse in the near-infrared window in biological tissues can facilitate wireless deep-brain stimulation for Parkinson's disease and pain management. Therefore, this study paves the way toward safe, ultraefficient, robust, configurable, and wireless optoelectronic bridges between inanimate and biological systems.

METHODS

Photoelectrode Fabrication. Photoelectrodes were fabricated on glass substrates covered with unpatterned indium tin oxide (ITO) (Ossila, S111). ITO-coated substrates were cleaned with NaOH solution for 5 min, tension-active agent in water solution (HELLMANEX II, 3%) for 15 min, deionized water for 15 min, pure acetone for 5 min, and isopropyl alcohol for 5 min, all at 55 °C, and then treated with UV−ozone for 25 min to eliminate any other residues on the ITO surface. P3HT (95.7% regioregular) and PCBM (>99% pure) were supplied by Ossilla and utilized without any further purification. The photoactive solution was prepared by mixing the donor material (P3HT) and the acceptor material (PCBM) with the optimized blending ratio of 1:0.6. P3HT and PCBM were prepared separately in *o*-dichlorobenzene with concentrations of 18.75 and 11.25 mg·mL^{-1}, respectively, stirred overnight at 70 °C, and then mixed and stirred for 3 h at 70 °C. The ZnO precursor solution was prepared by mixing 219.3 mg of zinc acetate dehydrate ($Zn(CH_3CO_2)_2{\cdot}2H_2O$) from Sigma-Aldrich in 2 mL of 2-methoxyethanol ($C_3H_8O_2$) and 80 mg of ethanolamine ($HOCH_2CH_2NH_2$) and sonicated for 2 h at 50 °C. The ZnO solution was filtered through a 0.45 μm PVDF filter, spin-coated onto the ITO substrates at 2000 rpm for 60 s, and annealed at 280 °C for 15 min. The photoactive layer was fabricated by spin-coating the P3HT:PCBM blend onto the ZnO layer at 400 rpm for 180 s and annealed at 150 °C for 10 min. The Au layer was coated on the photoactive layer using a thermal evaporator (Bruker, detail) at the rate of 0.02−0.04 nm·s^{-1} under 6.0 × 10−6 mbar vacuum pressure with 1, 5, 10, 15, and 30 nm thicknesses for the optimization procedure to maximize photocurrent generation. The thicknesses of the ZnO, P3HT:PCBM, and PEDOT:PSS layers are found to be 31, 225, and 140 nm, respectively (Figure S4), and the optimized Au layer is 10 nm thick.

We systematically varied the GOPS, EG, and DMSO concentration ratios in the PEDOT:PSS solution coated onto the ITO/ZnO/P3HT:PCBM/Au structure, at 1500 rpm for 60 s and annealed at 150 °C for 10 min, to maximize the non-faradic photocurrent without much increase in the faradic photocurrent. We prepared six types of photoelectrodes by changing the GOPS concentration in the PEDOT:PSS solution and fixing EG and DMSO concentrations to maximize the aqueous stability of the PEDOT:PSS biointerface layer. Once aqueous stability was achieved, EG and DMSO concentrations were methodically changed to increase the conductivity and coating uniformity of the PEDOT:PSS solution onto the Au layer.

Photocurrent Measurements. We characterized the optimized biointerface composed of different EG concentrations under different pulse conditions. Biointerfaces were illuminated from the top through the PEDOT:PSS interface layer with trains of 50 ms light pulses of blue, red, and green LEDs with nominal wavelengths at 445, 630, and 530 nm, respectively (Figure 2a). Measurement electrodes were not electrically grounded, and the reference electrode was directly contacted with the electrolyte to provide the characterization of the devices in a wireless and free-standing mode, which is the working condition of the implantable photovoltaic device in biological media. The control and biointerface devices were partially wiped out from the edges to uncover and use the ITO layer as the return electrode in

https://dx.doi.org/10.1021/acsami.0c11581
ACS Appl. Mater. Interfaces 2020, 12, 42997−43008

the measurement system. A patch-clamp amplifier was used for recording the photocurrent with the patch pipettes of ∼4 MΩ, which was kept close to the surface, with the reference electrode silver/silver chloride (Ag/AgCl) in the extracellular medium (aCSF) (Figure 2a). We investigated the combined effects of DMSO and EG concentrations in the PEDOT:PSS layer by evaluating the peak photocurrent and total charge injection for each enhancer combination (EG 0, 0.5, 1, 2, 5, 7, 10 vol %; DMSO 0, 2, 5, 7, 10, 12, 15 vol %). Concentrations of these additives were optimized for high capacitive current without increasing the faradic current. In particular, the capacitive photocurrent reached its maximum with 7 vol % DMSO and 2 vol % EG in the PEDOT:PSS solution (Figure 3a,c,d). These additive ratios were kept constant for the rest of the experiments to explore the benchmark values of the biointerface.

Photocurrent measurements were taken using an Olympus T2 upright microscope and an extracellular patch-clamp (EPC) 800 patch-clamp amplifier (HEKA Elektronik). An extracellular aCSF aqueous medium was prepared by mixing 10 mM 4-(2-hydroxyethyl)-1-piperazineethanesulfonic acid (HEPES, Sigma-Aldrich, 83264), 10 mM glucose, 2 mM $CaCl_2$, 140 mM NaCl, 1 mM $MgCl_2$, and 3 mM KC and mixed with distilled water, and the pH was calibrated to 7.4 using 1 M NaOH. Thorlab's blue (M450LP1), red (M625L4), and green (M530L3) LEDs were used as the light sources. The LED system was driven by DC2200—High-Power 1-Channel LED Driver with Pulse Modulation (Thorlab's). The photocurrent was measured without electrical grounding of the ITO layer, but the ground was connected to the electrolyte solution to mimic the biological environment that implantable devices are surrounded by.

Photoelectrochemical Measurements. Photoelectrochemical experiments were carried out using an Autolab Potentiostat Galvanostat PGSTAT (Metrhom, The Netherlands). A three-electrode system consisting of Ag/AgCl as the reference electrode, platinum wire as the counter electrode, and connection to the biointerface as the working electrode was used. All measurements were carried out at room temperature in an extracellular aCSF medium as the supporting electrolyte solution. The device was excited with blue, red, and green LEDs with optical power of 100 $mW{\cdot}cm^{-2}$. The optical power was measured with an optical power meter (Newport 843-R). The data were analyzed using NOVA software.

SH-SY5Y Cell Culture. The SH-SY5Y cell line was used in all electrophysiology experiments. SH-SY5Y cells were cultured in Dulbecco's modified Eagle's medium (DMEM, Gibco, 21969-035) supplemented with 10% fetal bovine serum (FBS, Gibco, 10500), 1% L-glutamine (Gibco, 25030-081), and 1% penicillin−streptomycin (Gibco, 15240-062). Cultures were maintained at 37 °C in a 5% CO_2, 85% humidified incubator. Cells were passaged and supplied with a fresh medium every 2−3 days.

Primary Astrocyte Isolation and Cell Culture. All experimental procedures were approved by the Institutional Animal Care and Use Committees of Koç University (Approval No. 2019.HADYEK.023) according to the Directive 2010/63/EU of the European Parliament and of the Council on the Protection of Animals Used for Scientific Purposes. The cortical tissues were extracted from decapitated E15−E17 Wistar Albino rats and were placed immediately in ice-cold HEPES buffered DMEM. The cortices were incubated in 0.25% Trypsin-EDTA solution (Thermo Fisher Scientific, 25200072) with 2% DNase-I supplement (NeoFroxx, 9003-98-9) for 25 min in a 37 °C incubator. Then, the cells were centrifuged, and the supernatant was changed with DMEM supplemented with 10% FBS and 1% penicillin/streptomycin. Then, the cell suspension was filtered through 120 and 45 μm nylon mesh filters, respectively. After filtration, the cell suspension was seeded to 250 mL noncoated culture flasks in 10 mL of DMEM with FBS. The cells were incubated at a 37 °C, 10% CO_2 atmosphere, and their medium was changed on day 3. On day 6, the cell culture medium was changed again, and the flasks were shaken overnight at 80 rpm at room temperature. The detached cells were washed with phosphate-buffered saline (PBS, Gibco, 10010031), and 10 mL of DMEM was added with FBS on attached cells in the flask. Cells were cultured at 37 °C, 10% CO_2, until they reached confluency. After confluency, the cells were trypsinized and seeded to poly-D-lysine (PDL, Sigma-Aldrich, P6407)-coated flasks in DMEM with FBS.[45]

Biocompatibility Tests. To investigate the cell viability and cell proliferation of SH-SY5Y cells and primary astrocytes on our biointerfaces, the MTT viability assay was used. The growth medium was prepared using Dulbecco's modified Eagle's medium with 10% heat-inactivated fetal bovine serum and antibiotics. The MTT cell viability assay (Abcam, ab211091) was utilized to evaluate the biocompatibility of our biointerface. The devices were sterilized first by cleaning with 70% ethanol followed by air-drying. The surface was further sterilized under UV irradiation for 30 min. The substrates were placed in six-well plates. SH-SY5Y cells were seeded (3×10^5 cells per well) on the substrates in DMEM with 10% FBS, and after 48 h of incubation, the medium was replaced with 1 mL of MTT solution (5 $mg{\cdot}mL^{-1}$ in PBS, pH = 7.4) and 4 mL of DMEM mixture per well. Concurrently, primary astrocytes were seeded (2×10^5 cells per well) on the substrates in DMEM with 10% FBS, and after 72 h of incubation, which is the sufficient time to induce innate immune response, the medium was replaced with 1 mL of MTT solution (5 $mg{\cdot}mL^{-1}$ in PBS, pH = 7.4) and 4 mL of DMEM mixture per well. Then, for an additional 4 h, the cells were incubated at a 37 °C, 5% CO_2 atmosphere. The medium was vacuumed from each well, and substrates were transferred to an empty six-well plate. In each well, a 1:1 mixture of DMSO and ethanol was added to dissolve the formazan crystals. The solution was transferred to a 96-well plate, and the absorbance was measured at 600 nm (for background) and at 690 nm (for absorbance) with a Synergy H1Micro-plate Reader (Bio-Tek Instruments). The relative cell viability was calculated as follows: viability = $(OD_{sample}/OD_{control}) \times 100$. The optical density (OD) of the sample was obtained from the cells grown on a photoelectrode, and the OD of the control was obtained from the cells grown on the ITO substrates.

Immunofluorescence Staining and Imaging. SH-SY5Y cells (2.5×10^5 cells per sample) were seeded on the ITO control substrate and the biointerface and incubated for 48 h at 37 °C in a cell culture incubator. Primary astrocytes (2×10^5 cells per sample) were seeded on the ITO control substrate and the biointerface in a similar way and incubated for 72 h at 37 °C in a cell culture incubator. After incubation, both cells were fixed by 4% paraformaldehyde and washed three times with PBS-T (phosphate-buffered saline, 0.1% Triton X-100). Cells were blocked in PBS solution containing 5% BSA (bovine serum albumin) and 0.1% Triton X-100. SH-SY5Y samples were incubated with the mouse anti-β-III tubulin primary antibody (Sigma-Aldrich, T8578) 2 h and washed three times with PBS-T. Primary astrocyte samples were incubated with rabbit anti-GFAP (Abcam, ab7260) and rabbit antivimentin (Abcam, ab92547) primary antibodies overnight, as selective markers of astrocytes, and washed three times with PBS-T. For visualization of the cytoskeleton, SH-SY5Y samples were incubated with the goat antimouse IgG H&L Alexa Fluor 488 secondary antibody (Abcam, ab150113) with DAPI (D1306, Sigma), and primary astrocyte samples were incubated with the FITC-conjugated phalloidin antibody (Sigma-Aldrich, P5282) for 90 min at 37 °C. Astrocyte samples were incubated with goat antirabbit IgG H&L Alexa Fluor 555 (Cell Signaling Technology, 4413) and goat antirabbit IgG H&L Alexa Fluor 647 (Abcam, ab150079) secondary antibodies for fluorophore markings of anti-GFAP and antivimentin primary antibodies for 90 min at 37 °C, respectively. All samples were washed three times with PBS-T and then mounted with a DAPI-supplemented mounting medium (Abcam, ab104139) to observe nuclei. Finally, immunofluorescence imaging was done using fluorescence (Axio Observer Z1, Zeiss) and confocal (TCS SP8 DLS, Leica) microscopes.

Electrophysiology Experiments. Electrophysiology experiments were performed by the EPC 800 patch-clamp amplifier (HEKA Elektronik). The biointerface was cleaned with 70 vol % ethanol solution and incubated for 3 days in DI water. The pulled patch pipettes of 4−6 MΩ were used to conduct the whole-cell patch-clamp experiment. The extracellular medium (aCSF) was prepared as previously mentioned. The internal cellular medium was prepared by mixing 140 mM KCl, 2 mM $MgCl_2$, 10 mM HEPES, 10 mM ethylene

https://dx.doi.org/10.1021/acsami.0c11581
ACS Appl. Mater. Interfaces 2020, 12, 42997−43008

glycol-bis(β-aminoethyl ether)-*N*,*N*,*N*′,*N*′-tetraacetic acid (EGTA), and 2 mM Mg-ATP in water, and the pH was calibrated to 7.2−7.3 using 1 M KOH. Patch pipettes were filled with the intracellular solution. A digital-camera-integrated Olympus T2 upright microscope was used to patch and monitor the cells. The whole-cell patched cells were observed up to 1 h to investigate the possible damage done by patched pipettes.

PHOTOTHERMAL EFFECT DUE TO LIGHT ILLUMINATION

Using the thermodynamic relation

$$d_p(\text{rev}, p) = mC_p dT \quad (1)$$

$$\int_q^0 d_p(\text{rev}, p) = mC_p \int_T^{295\ \text{K}} dT \quad (2)$$

Using the water heat capacity C_p = 75.291 J·K^{-1}·mol^{-1}, the specific heat capacity can be calculated as

$$q = mC_p \Delta T \quad (3)$$

On the other hand, the thermal energy (q) due to light illumination

$$q = I \times t = 1\ \text{s} \times 100\ \text{mW} = 100\ \text{mJ} \quad (4)$$

where I is the light illumination power (100 mW) and t is the illumination time (1 s). Using eqs 3 and 4

$$(0.0332\ \text{g}/18\ \text{g/mol}) \times 75.291\ \text{J K}^{-1}\text{mol}^{-1}\ \Delta T,\ \Delta T = 0.728\ ^\circ\text{C} \quad (5)$$

ASSOCIATED CONTENT

Supporting Information

The Supporting Information is available free of charge at https://pubs.acs.org/doi/10.1021/acsami.0c11581.

Photocurrent gradient from the surface; fluorescence microscopy after DAPI staining; phase-contrast microscope imaging of SH-SY5Y cells; phase-contrast microscope images of primary astrocytes; cross-sectional SEM image (PDF)

AUTHOR INFORMATION

Corresponding Author

Sedat Nizamoglu − *Department of Electrical and Electronics Engineering and Graduate School of Biomedical Sciences and Engineering, Koc University, Istanbul 34450, Turkey;* orcid.org/0000-0003-0394-5790; Email: snizamoglu@ku.edu.tr

Authors

Mertcan Han − *Department of Electrical and Electronics Engineering, Koc University, Istanbul 34450, Turkey;* orcid.org/0000-0002-3543-5894

Shashi Bhushan Srivastava − *Department of Electrical and Electronics Engineering, Koc University, Istanbul 34450, Turkey*

Erdost Yildiz − *Koc University Research Center for Translational Medicine, Koc University, Istanbul 34450, Turkey;* orcid.org/0000-0001-8086-3524

Rustamzhon Melikov − *Department of Electrical and Electronics Engineering, Koc University, Istanbul 34450, Turkey;* orcid.org/0000-0003-2214-7604

Saliha Surme − *Molecular Biology and Genetics, College of Science, Koc University, Istanbul 34450, Turkey*

Itir Bakis Dogru-Yuksel − *Graduate School of Biomedical Sciences and Engineering, Koc University, Istanbul 34450, Turkey;* orcid.org/0000-0001-8569-7625

Ibrahim Halil Kavakli − *Molecular Biology and Genetics, College of Science and College of Engineering, Chemical and Biological Engineering, Koc University, Istanbul 34450, Turkey;* orcid.org/0000-0001-6624-3505

Afsun Sahin − *Koc University Research Center for Translational Medicine, Koc University, Istanbul 34450, Turkey; Department of Ophthalmology, Medical School Koc University, Istanbul 34450, Turkey*

Complete contact information is available at: https://pubs.acs.org/10.1021/acsami.0c11581

Author Contributions

M.H. planned the experiments, fabricated the biointerfaces, performed photostimulation, photoelectrochemical, and electrophysiological experiments, analyzed the data, and wrote the manuscript. S.B.S. fabricated the biointerfaces, performed photostimulation experiments, and analyzed the data. E.Y. prepared the primary astrocyte cell cultures, performed cell viability assays and immunofluorescence staining experiments, analyzed the data, and wrote the manuscript. R.M. prepared the photostimulation setup and discussed the results. S.S. prepared the SH-SY5Y cell cultures, performed cell viability assays and fluorescence microscopy experiments, and analyzed the data. I.B.D.-Y. prepared the electrophysiology setup. I.H.K. and A.S. interpreted and discussed the data and supervised the cell culture, cell viability assays, and fluorescence microscopy experiments. S.N. planned the experiments, interpreted and discussed the data, initiated the study, and wrote the manuscript. All of the authors have read, edited, and accepted the manuscript.

Notes

The authors declare no competing financial interest.

All data needed to evaluate the conclusions in the paper are present in the paper. Additional data related to this paper may be requested from the corresponding author upon reasonable request.

ACKNOWLEDGMENTS

This project has received funding from the European Research Council (ERC) under the European Union's Horizon 2020 Research and Innovation Programme (grant agreement no. 639846). S.N. also acknowledges the support by the Turkish Academy of Sciences (TÜBA-GEBIP; The Young Scientist Award Program) and the Science Academy of Turkey (BAGEP; The Young Scientist Award Program). The authors gratefully acknowledge use of the services and facilities of the Koç University Research Center for Translational Medicine (KUTTAM), funded by the Republic of Turkey Ministry of Development. The content is solely the responsibility of the authors and does not necessarily represent the official views of the Ministry of Development.

REFERENCES

(1) Zhang, M.; Tang, Z.; Liu, X.; Van der Spiegel, J. Electronic Neural Interfaces. *Nat. Electron.* **2020**, 3, 191−200.

(2) Kringelbach, M. L.; Jenkinson, N.; Owen, S. L. F.; Aziz, T. Z. Translational Principles of Deep Brain Stimulation. *Nat. Rev. Neurosci.* **2007**, 623−635.

(3) Grossman, N.; Bono, D.; Dedic, N.; Kodandaramaiah, S. B.; Rudenko, A.; Suk, H. J.; Cassara, A. M.; Neufeld, E.; Kuster, N.; Tsai,

L. H.; Pascual-Leone, A.; Boyden, E. S. Noninvasive Deep Brain Stimulation via Temporally Interfering Electric Fields. *Cell* **2017**, *169*, 1029−1041. 1029-1041

(4) Fu, T. M.; Hong, G.; Zhou, T.; Schuhmann, T. G.; Viveros, R. D.; Lieber, C. M. Stable Long-Term Chronic Brain Mapping at the Single-Neuron Level. *Nat. Methods* **2016**, *13*, 875−882.

(5) Fasano, A.; Daniele, A.; Albanese, A. Treatment of Motor and Non-Motor Features of Parkinson's Disease with Deep Brain Stimulation. *Lancet Neurol.* **2012**, *11*, 429−442.

(6) Freed, L. E.; Engelmayr, G. C.; Borenstein, J. T.; Moutos, F. T.; Guilak, F. Advanced Material Strategies for Tissue Engineering Scaffolds. *Adv. Mater.* **2009**, *21*, 3410−3418.

(7) Mathieson, K.; Loudin, J.; Goetz, G.; Huie, P.; Wang, L.; Kamins, T. I.; Galambos, L.; Smith, R.; Harris, J. S.; Sher, A.; Palanker, D. Photovoltaic Retinal Prosthesis with High Pixel Density. *Nat. Photonics* **2012**, *6*, 391−397.

(8) Bareket-Keren, L.; Hanein, Y. Novel Interfaces for Light Directed Neuronal Stimulation: Advances and Challenges. *Int. J. Nanomed.* **2014**, *9*, 65−83.

(9) Feiner, R.; Dvir, T. Tissue-Electronics Interfaces: From Implantable Devices to Engineered Tissues. *Nat. Rev. Mater.* **2017**, *28*, 1−16.

(10) Bahmani Jalali, H.; Aria, M. M.; Dikbas, U. M.; Sadeghi, S.; Kumar, B. G.; Sahin, M.; Kavakli, I. H.; Ow-Yang, C. W.; Nizamoglu, S. Effective Neural Photostimulation Using Indium-Based Type-II Quantum Dots. *ACS Nano* **2018**, *12*, 8104−8114.

(11) Bahmani Jalali, H.; Karatum, O.; Melikov, R.; Dikbas, U. M.; Sadeghi, S.; Yildiz, E.; Dogru, I. B.; Eren, G. O.; Ergun, C.; Sahin, A.; Kavakli, I. H.; Nizamoglu, S. Biocompatible Quantum Funnels for Neural Photostimulation. *Nano Lett.* **2019**, *19*, 5975−5981.

(12) Jiang, Y.; Li, X.; Liu, B.; Yi, J.; Fang, Y.; Shi, F.; Gao, X.; Sudzilovsky, E.; Parameswaran, R.; Koehler, K.; Nair, V.; Yue, J.; Guo, K. H.; Fang, Y.; Tsai, H. M.; Freyermuth, G.; Wong, R. C. S.; Kao, C. M.; Chen, C. T.; Nicholls, A. W.; Wu, X.; Shepherd, G. M. G.; Tian, B. Rational Design of Silicon Structures for Optically Controlled Multiscale Biointerfaces. *Nat. Biomed. Eng.* **2018**, *2*, 508−521.

(13) Ghezzi, D.; Antognazza, M. R.; MacCarone, R.; Bellani, S.; Lanzarini, E.; Martino, N.; Mete, M.; Pertile, G.; Bisti, S.; Lanzani, G.; Benfenati, F. A Polymer Optoelectronic Interface Restores Light Sensitivity in Blind Rat Retinas. *Nat. Photonics* **2013**, *7*, 400−406.

(14) Jakešová, M.; Silverå Ejneby, M.; Đerek, V.; Schmidt, T.; Gryszel, M.; Brask, J.; Schindl, R.; Simon, D. T.; Berggren, M.; Elinder, F.; Głowacki, E. D. Optoelectronic Control of Single Cells Using Organic Photocapacitors. *Sci. Adv.* **2019**, *5*, No. eaav5265.

(15) Ghezzi, D.; Antognazza, M. R.; Dal Maschio, M.; Lanzarini, E.; Benfenati, F.; Lanzani, G. A Hybrid Bioorganic Interface for Neuronal Photoactivation. *Nat. Commun.* **2011**, *2*, No. 166.

(16) Rand, D.; Jakešová, M.; Lubin, G.; Vėbraitė, I.; David-Pur, M.; Đerek, V.; Cramer, T.; Sariciftci, N. S.; Hanein, Y.; Głowacki, E. D. Direct Electrical Neurostimulation with Organic Pigment Photocapacitors. *Adv. Mater.* **2018**, *30*, No. 1707292.

(17) Srivastava, S. B.; Melikov, R.; Aria, M. M.; Dikbas, U. M.; Kavakli, I. H.; Nizamoglu, S. Band Alignment Engineers Faradaic and Capacitive Photostimulation of Neurons Without Surface Modification. *Phys. Rev. Appl.* **2019**, *11*, 12.

(18) Srivastava, S.; Melikov, R.; Yildiz, E.; Han, M.; Sahin, A.; Nizamoglu, S. Efficient Photocapacitors via Ternary Hybridphotovoltaic Optimization for Photostimulationof Neurons. *Biomed. Opt. Express* **2020**, *11*, 5237.

(19) Wang, G.; Zhang, L.; Zhang, J. A Review of Electrode Materials for Electrochemical Supercapacitors. *Chem. Soc. Rev.* **2012**, *41*, 797−828.

(20) He, H.; Zhang, L.; Guan, X.; Cheng, H.; Liu, X.; Yu, S.; Wei, J.; Ouyang, J. Biocompatible Conductive Polymers with High Conductivity and High Stretchability. *ACS Appl. Mater. Interfaces* **2019**, *11*, 26185−26193.

(21) Na, S.-I.; Kim, S.-S.; Jo, J.; Kim, D.-Y. Efficient and Flexible ITO-Free Organic Solar Cells Using Highly Conductive Polymer Anodes. *Adv. Mater.* **2008**, *20*, 4061−4067.

(22) Bryan, A. M.; Santino, L. M.; Lu, Y.; Acharya, S.; D'Arcy, J. M. Conducting Polymers for Pseudocapacitive Energy Storage. *Chem. Mater.* **2016**, *28*, 5989−5998.

(23) Khodagholy, D.; Doublet, T.; Gurfinkel, M.; Quilichini, P.; Ismailova, E.; Leleux, P.; Herve, T.; Sanaur, S.; Bernard, C.; Malliaras, G. G. Highly Conformable Conducting Polymer Electrodes for In Vivo Recordings. *Adv. Mater.* **2011**, *23*, H268−H272.

(24) Khodagholy, D.; Gelinas, J. N.; Zhao, Z.; Yeh, M.; Long, M.; Greenlee, J. D.; Doyle, W.; Devinsky, O.; Buzsáki, G. Organic Electronics for High-Resolution Electrocorticography of the Human Brain. *Sci. Adv.* **2016**, *2*, No. e1601027.

(25) Hu, Z.; Zhang, J.; Hao, Z.; Zhao, Y. Influence of Doped PEDOT:PSS on the Performance of Polymer Solar Cells. *Sol. Energy Mater. Sol. Cells* **2011**, *95*, 2763−2767.

(26) Maya-Vetencourt, J. F.; Ghezzi, D.; Antognazza, M. R.; Colombo, E.; Mete, M.; Feyen, P.; Desii, A.; Buschiazzo, A.; Di Paolo, M.; Di Marco, S.; Ticconi, F.; Emionite, L.; Shmal, D.; Marini, C.; Donelli, I.; Freddi, G.; MacCarone, R.; Bisti, S.; Sambuceti, G.; Pertile, G.; Lanzani, G.; Benfenati, F. A Fully Organic Retinal Prosthesis Restores Vision in a Rat Model of Degenerative Blindness. *Nat. Mater.* **2017**, *16*, 681−689.

(27) ElMahmoudy, M.; Inal, S.; Charrier, A.; Uguz, I.; Malliaras, G. G.; Sanaur, S. Tailoring the Electrochemical and Mechanical Properties of PEDOT:PSS Films for Bioelectronics. *Macromol. Mater. Eng.* **2017**, *302*, No. 1600497.

(28) Lingstedt, L. V.; Ghittorelli, M.; Lu, H.; Koutsouras, D. A.; Marszalek, T.; Torricelli, F.; Crăciun, N. I.; Gkoupidenis, P.; Blom, P. W. M. Effect of DMSO Solvent Treatments on the Performance of PEDOT:PSS Based Organic Electrochemical Transistors. *Adv. Electron. Mater.* **2019**, *5*, No. 1800804.

(29) Schoen, I.; Fromherz, P. Extracellular Stimulation of Mammalian Neurons Through Repetitive Activation of Na Channels by Weak Capacitive Currents on a Silicon Chip. *J. Neurophysiol.* **2008**, *100*, 346−357.

(30) Merrill, D. R.; Bikson, M.; Jefferys, J. G. R. Electrical Stimulation of Excitable Tissue: Design of Efficacious and Safe Protocols. *J. Neurosci. Methods* **2005**, 171−198.

(31) Schoen, I.; Fromherz, P. The Mechanism of Extracellular Stimulation of Nerve Cells on an Electrolyte-Oxide-Semiconductor Capacitor. *Biophys. J.* **2007**, *92*, 1096−1111.

(32) Silverå Ejneby, M.; Migliaccio, L.; Gicevičius, M.; Đerek, V.; Jakešová, M.; Elinder, F.; Głowacki, E. D. Extracellular Photovoltage Clamp Using Conducting Polymer-Modified Organic Photocapacitors. *Adv. Mater. Technol.* **2020**, *5*, No. 1900860.

(33) Jacques, S. L. Optical Properties of Biological Tissues: A Review. *Phys. Med. Biol.* **2013**, *58*, R37−R61.

(34) Cogan, S. F. Neural Stimulation and Recording Electrodes. *Annu. Rev. Biomed. Eng.* **2008**, *10*, 275−309.

(35) Moshayedi, P.; Ng, G.; Kwok, J. C. F.; Yeo, G. S. H.; Bryant, C. E.; Fawcett, J. W.; Franze, K.; Guck, J. The Relationship between Glial Cell Mechanosensitivity and Foreign Body Reactions in the Central Nervous System. *Biomaterials* **2014**, *35*, 3919−3925.

(36) He, H.; Zhang, L.; Guan, X.; Cheng, H. L.; Liu, X. X.; Yu, S. Z.; Wei, J.; Ouyang, J. Y. Biocompatible Conductive Polymers with High Conductivity and High Stretchability. *ACS Appl. Mater. Interfaces* **2019**, *11*, 26185−26193.

(37) Abdullaeva, O. S.; Schulz, M.; Balzer, F.; Parisi, J.; Lützen, A.; Dedek, K.; Schiek, M. Photoelectrical Stimulation of Neuronal Cells by an Organic Semiconductor-Electrolyte Interface. *Langmuir* **2016**, *32*, 8533−8542.

(38) Abdullaeva, O. S.; Balzer, F.; Schulz, M.; Parisi, J.; Lützen, A.; Dedek, K.; Schiek, M. Organic Photovoltaic Sensors for Photocapacitive Stimulation of Voltage-Gated Ion Channels in Neuroblastoma Cells. *Adv. Funct. Mater.* **2019**, *29*, No. 1805177.

(39) Melikov, R.; Srivastava, S. B.; Karatum, O.; Dogru-Yuksel, I. B.; Bahmani Jalali, H.; Sadeghi, S.; Dikbas, U. M.; Ulgut, B.; Kavakli, I. H.; Cetin, A.; Nizamoğlu, S. Plasmon-Coupled Photocapacitor Neuromodulators. *ACS Appl. Mater. Interfaces* **2020**, *12*, 35940.

https://dx.doi.org/10.1021/acsami.0c11581
ACS Appl. Mater. Interfaces 2020, 12, 42997−43008

(40) Rand, D.; Jakešová, M.; Lubin, G.; Vėbraitė, I.; David-Pur, M.; Đerek, V.; Cramer, T.; Sariciftci, N. S.; Hanein, Y.; Głowacki, E. D. Direct Electrical Neurostimulation with Organic Pigment Photocapacitors. *Adv. Mater.* **2018**, *30*, No. 1707292.
(41) Hermann, J. K.; Capadona, J. R. Understanding the Role of Innate Immunity in the Response to Intracortical Microelectrodes. *Crit. Rev. Biomed. Eng.* **2018**, *46*, 341−367.
(42) Khodagholy, D.; Gelinas, J. N.; Thesen, T.; Doyle, W.; Devinsky, O.; Malliaras, G. G.; Buzsáki, G. NeuroGrid: Recording Action Potentials from the Surface of the Brain. *Nat. Neurosci.* **2015**, *18*, 310−315.
(43) Khodagholy, D.; Rivnay, J.; Sessolo, M.; Gurfinkel, M.; Leleux, P.; Jimison, L. H.; Stavrinidou, E.; Herve, T.; Sanaur, S.; Owens, R. M.; Malliaras, G. G. High Transconductance Organic Electrochemical Transistors. *Nat. Commun.* **2013**, *4*, No. 2133.
(44) Bryan, A. M.; Santino, L. M.; Lu, Y.; Acharya, S.; D'Arcy, J. M. Conducting Polymers for Pseudocapacitive Energy Storage. *Chem. Mater.* **2016**, *28*, 5989−5998.
(45) Gaillard, P. J.; Voorwinden, L. H.; Nielsen, J. L.; Ivanov, A.; Atsumi, R.; Engman, H.; Ringbom, C.; De Boer, A. G.; Breimer, D. D. Establishment and Functional Characterization of an in Vitro Model of the Blood-Brain Barrier, Comprising a Co-Culture of Brain Capillary Endothelial Cells and Astrocytes. *Eur J. Pharm. Sci.* **2001**, *12*, 215−222.

https://dx.doi.org/10.1021/acsami.0c11581
ACS Appl. Mater. Interfaces 2020, 12, 42997−43008